Contents lists available at ScienceDirect

Physics of the Earth and Planetary Interiors

journal homepage: www.elsevier.com/locate/pepi

Earthquake location based on Distributed Acoustic Sensing (DAS) as a seismic array

K. Lentas [a],[*], D. Bowden [b], N.S. Melis [a], A. Fichtner [b], M. Koroni [c], K. Smolinski [b], A. Bogris [d], T. Nikas [e], C. Simos [f], I. Simos [g]

[a] *National Observatory of Athens, Institute of Geodynamics, Lofos Nymfon, Athens 11810, Greece*
[b] *Department of Earth Sciences, ETH Zurich, Zurich, Switzerland*
[c] *Swiss Seismological Service, ETH Zurich, Zurich CH-8092, Switzerland*
[d] *Department of Informatics and Computer Engineering, University of West Attica, Aghiou Spiridonos, Egaleo 12243, Greece*
[e] *Department of Informatics and Telecommunications, National and Kapodistrian University of Athens, Athens 15784, Greece*
[f] *Electronics and Photonics Laboratory, Department of Physics, University of Thessaly, Lamia 35100, Greece*
[g] *Department of Electrical and Electronics Engineering, University of West Attica, Egaleo 12243, Greece*

ARTICLE INFO

ABSTRACT

We present a simple and fast method to estimate preliminary earthquake location coordinates using Distributed Acoustic Sensing (DAS). Strain rate data is recorded on a 25-km long fibre-optic cable located in the northern suburbs of Athens (Greece). We apply frequency - wavenumber analysis on two segments of the cable forming an L-shaped seismic array, which offers good azimuthal sensitivity, whereas, the spatial resolution (spacing) and signal coherency control the ability to reliably resolve the apparent slowness of an incoming wavefield, and hence, to estimate the hypocentral distance to the array. We attempt to locate a local earthquake (2021/9/23, M_L=3.4, Thiva) NW to the DAS array (approximately 50 km NW of Athens), and a regional earthquake (2021/10/12, M_W=6.3, off the East coast of Crete) using S-wave onsets filtered within two frequency bands (0.5 Hz - 2.5 Hz and 1.0 Hz - 5.0 Hz). The obtained backazimuths agree with the observed backazimuths based on the locations reported by the Institute of Geodynamics, National Observatory of Athens (NOA) for both earthquakes, with our location for the local earthquake being roughly 10 km South of the NOA location, whereas, the location that we obtained for the regional earthquake suggested larger errors in distance, projected in our slowness estimation, possibly due to the array spatial resolution and the complex structure of the Hellenic subduction zone.

1. Introduction

Distributed Acoustic Sensing (DAS) systems offer an innovative way to measure the strain rate along a fibre-optic cable, by monitoring phase changes in Rayleigh backscattered light generated by a sequence of short duration laser pulses (~ 10 ns, Hartog, 2017; Lindsey and Martin, 2021). Even though the first applications with Earth science context were in reservoir monitoring (geothermal, hydrocarbons, Mateeva et al., 2012; Daley et al., 2013), it soon ignited the interest of the seismological community, as a result of the ease of deploying cables in certain environments (e.g., on glaciers and/or volcanoes, Booth et al., 2020; Klaasen et al., 2021), the possibility to co-use telecom cables, the wide frequency range of the recorded signals (Lindsey et al., 2020; Paitz et al., 2020), as

well as its relatively low noise level even in submarine applications (Ide et al., 2021).

The widespread coverage of fibre-optic cables across the Earth, has paved new ways in earthquake monitoring, especially in densely populated cities, where the deployment of seismic instruments can be challenging, primarily due to permission restrictions at urban sites, as well as security issues and high cost of maintenance. The use of DAS on commercially deployed fibre-optic cables and dark fibres, has revealed its ability to record a great variety of seismic signals such as earthquakes, thunderquakes, icequakes, anthropogenic sources, traffic in urban areas, live music (i.e. Spica et al., 2020; Nishimura et al., 2021; van den Ende and Ampuero, 2021; Zhu et al., 2021), as well as hydracoustic signals on water basin deployed cables (Matsumoto et al., 2021). As a result, a

---

plethora of seismological studies has recently been published in earthquake monitoring and source characterisation (i.e. Ajo-Franklin et al., 2019; Hudson et al., 2021; Lior et al., 2021; Agostinetti et al., 2022), structural imaging (Jousset et al., 2018), and the study of shallow structure and site characterisation in urban (i.e. Fang et al., 2020; Spica et al., 2020; Song et al., 2021) and volcanic environments (i.e. Nishimura et al., 2021; Fichtner et al., 2022).

Since DAS provides discrete locations of strain rate recordings with constant spacing on the order of 1 m along 10s of kilometers, its use as a seismic array seems to be appealing. Several studies have shown the benefits and challenges of using DAS arrays in seismic monitoring and earthquake location (i.e. Lindsey et al., 2017; Li et al., 2018; van den Ende and Ampuero, 2021). On the other hand, seismic arrays have been proven to be excellent tools in routine earthquake detection and monitoring for decades (i.e. Kværna and Ringdal, 1986; Mykkeltveit et al., 1990; Schweitzer and Krüger, 2011; Meng et al., 2014), as well as offering valuable information in earthquake source propagation characterisations (Ishii et al., 2005).

In this study, we use strain rate waveforms recorded on a Silixa iDAS interrogator, which was installed in Greece, at the premises of the OTE Academy (Hellenic Telecommunications Organisation), in Marousi (North of Athens), from late September to mid October 2021, connected to a roughly 25-km long fibre-optic cable with a gauge length of 10 m and a two-metres spatial resolution, totalling 12,416 channels (Fig. 1a). The main objective of this deployment was local earthquake detection and shallow structure imaging, and secondly, the comparison of a newly developed system, the so-called, Microwave Frequency Fibre Interferometer (MFFI) against the Silixa iDAS interrogator as a benchmark (Bogris et al., 2022; Bowden et al., 2022). During this period of time, several local and regional earthquakes were recorded, and their hypocentral parameters were listed in the Bulletin of the Institute of Geodynamics (NOA) (https://www.gein.noa.gr/en/services-products/database-search/). Here, we use part of the DAS recordings as an L-shaped seismic array, and we determine the epicentral coordinates of a local earthquake (2021/09/23, M_L=3.4, Thiva) and a regional earthquake (2021/10/12, M_W=6.3, off the East coast of Crete), without the use of additional seismic waveforms or parametric data.

2. Commercial fibre-optic cable as a DAS seismic array

We carried out several hammer tap tests in order to map the exact path of the cable, and as a result, we determined the coordinates of the discrete DAS channels. The first hammer tap points at the adjacent street outside the OTE Academy building were observed approximately at 800 m distance along the fibre, hence, part of the cable prior to this is expected to lie inside the walls of the building, where distributing racks and strong bends would not allow any observations. In fact, this is in agreement with raw DAS recordings where even strong earthquakes were not observed in the first ∼400 m of the cable (see for example Fig. S1 in the supplementary material).

For the purpose of this study, we focus on the southern part of the cable within the Marousi area, from 810 m to 5000 m (Fig. 1b and c) which is easily accessible and for which we have mapped the exact locations of telecommunication manholes and distributing boxes. We test the coherency of the strain rate signals, by cross-correlating waveforms of each channel to each other every 10 m. We first removed the mean and linear trend, a Hanning taper was applied and the waveform data was filtered from 0.5 Hz to 2.5 Hz. The timeseries were cut 5 s prior to the first arrival and 5 s after the signal was roughly at the same level as the noise. The waveforms were then normalised in amplitude, and the correlation coefficient was calculated, by measuring the shift over a predefined number of samples.

Two segments of the highest signal coherency are observed, the first ranges from 1000 m to 2350 m, and the second from 2350 m to 3300 m approximately, with an instant break in coherency at 2350 m. At roughly 1750 m, there is a sudden drop of coherency as a result of a U-turn, where the cable crosses the street to the other side, as witnessed by the marks on the street. Moreover, at approximately 2350 m the cable turns 90° to the south-east and follows a small roundabout. Telecommunication manholes and distributing boxes are spread regularly along the cable's path which may also be associated with low signal coherency and/or dead channels (Wuestefeld and Wilks, 2019).

Based on the coherency performance of the fibre-optic cable we choose to use the first two linear segments of the cable from 810 m to 2300 m (SW-NE orientation), and from 2300 m to 3500 m (NW-SE orientation), as an L-shaped array, setting the spacing of the array to 10 m. First we calculated the transfer function for each of the two linear segments, based on a concept valid for conventional three-component seismic arrays which indicates the resolution and sensitivity of a plane wave in frequency-slowness domain (Schweitzer et al., 2012). As seen in Fig. 2 (a and b), both linear segments show sensitivity perpendicular to their orientations. By combining the two linear segments into an L-shaped array, the transfer function becomes approximately an ellipse (Fig. 2c), providing good azimuthal resolution. Nevertheless, in DAS applications the fibre-optic cable is most sensitive along the cable axis for P-waves and for S-waves arriving broadside to the cable. This directivity effect and its implications to the overall response of a DAS array are well documented in Näsholm et al. (2022). Specifically, they argue that L-shaped DAS arrays exhibit an angular dependence in their response, but can still be useful in many applications. This can be of great importance when designing and optimising array geometries for seismic experiments. In our work, we make use of a pre-deployed cable in urban environment serving the local telecommunication network, rather than deploying a cable based on an optimal geometry. For this reason, we decided to use two linear segments which are perpendicular to each other, in order to reduce any directivity effects from the cable being too straight.

3. Methodology

We used raw strain rate DAS waveform data (processed in the same way as described in the previous section, see also the Results section for more details on the filtering) in order to compute the epicentral latitude (φ) and longitude (λ) of a seismic event with respect to the centre (φ_c, λ_c) of the L-shaped DAS array presented in the previous section. The central point of the array simply corresponds to the mean latitude and longitude with respect to each component of the array.

We followed the frequency - wavenumber (f-k) method (Capon et al., 1967; Aki and Richards, 1981) to compute beams within a certain range of different apparent slowness vectors ($s_{app.}$) and small steps of back-azimuth ($\widehat{b}$). The method is based on the assumption that each discrete sensor of an array will record a seismic signal which samples the medium from the source to each sensor, showing high coherency with each other. Since the wavefront will reach each sensor at slightly different distance and azimuth, delay times for each sensor are calculated for different backazimuth and apparent velocity combinations, which are then used in a delay and sum process to calculate the beam of the array. In simple words, we search for the $\widehat{b}$ - $s_{app.}$ pair that provides the maximum energy of the beam, whilst, in f-k analysis the process is done in the frequency-wavenumber domain where a phase shift is equivalent to a time shift in the time domain. A thorough discussion of the f-k method is presented for example in Schweitzer et al. (2012).

After we have defined the backazimuth that provided the maximum beam energy, we measured the travel time differences of first P/S phase arrivals in the central point of the array, and we attempted to fit theoretical travel time differences for P/S, p/s and P_n/S_n phases for fixed depth values (i.e., for shallow events from 0 km to 50 km), in order to estimate the epicentral distance on a 1D Earth (Kennett et al., 1995). In order to avoid any acausal effects on the signal as a result of the filtering (the more impulsive the signal, the larger the effect) the onset time arrivals where picked on raw strain rate data. Once the backazimuth and
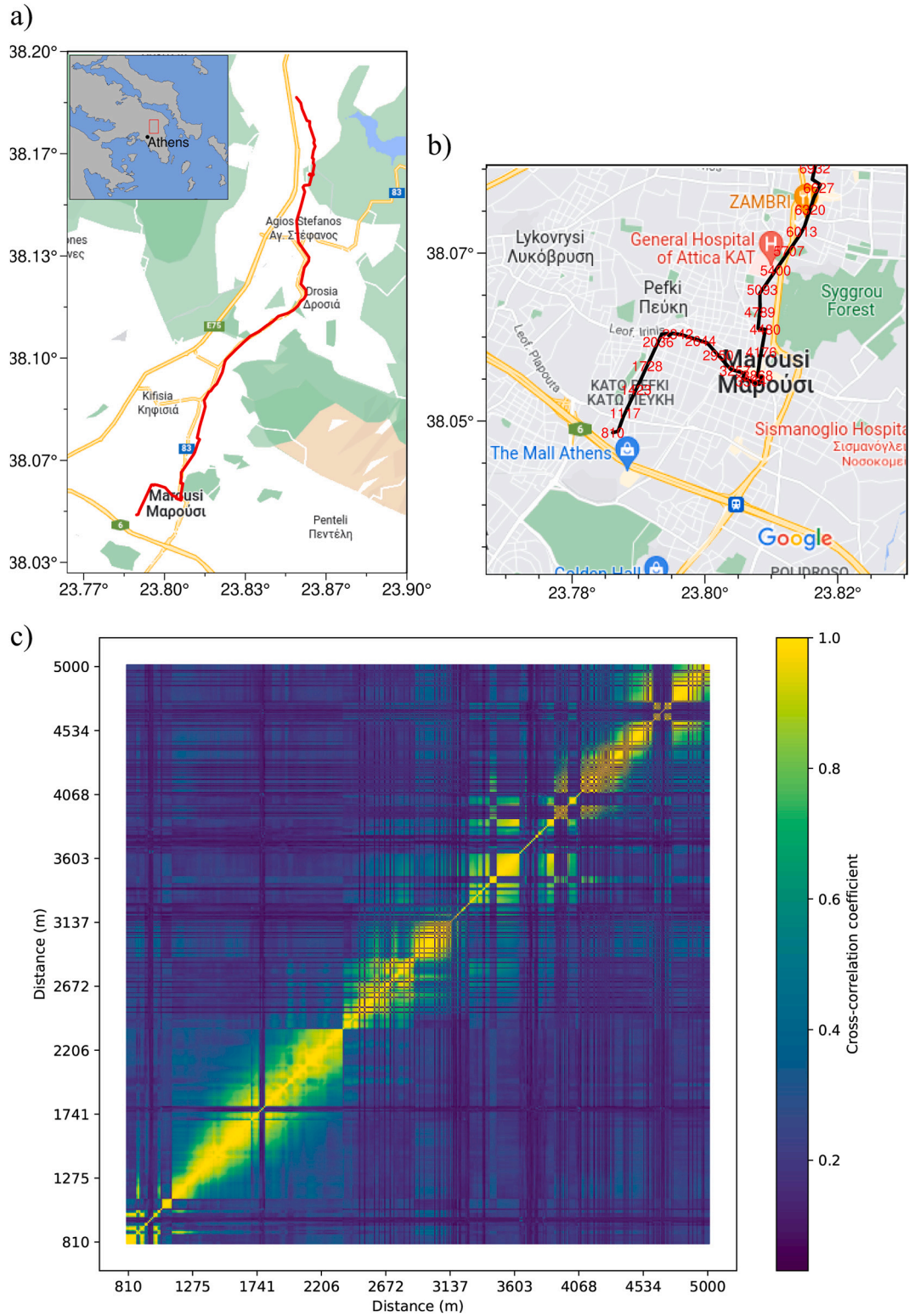
Fig. 1. (a) A Google map showing the trace (in red) of the fibre-optic cable used in this study. The red rectangle on the inlet map shows the location of the fibre-optic cable with respect to the broad area of Athens, Greece; (b) A Google map focusing on the southern part of the fibre-optic cable used in this study and its associated strain rate coherence matrix (c). The trace of the fibre-optic cable in "b" is shown in black on the map and the distances across the cable are shown in red as determined by several tapping tests. (For interpretation of the references to colour in this figure legend, the reader is referred to the web version of this article.)

the epicentral distance were defined, the epicentral coordinates with respect to the centre of the array were obtained for any fixed depth (i.e., Pirli et al., 2006) based on great circles (Karney, 2012).

4. Results

In order to assess the location accuracy for the simple method described in the previous section, with respect to the noise level in the waveforms, we first applied synthetic tests based on a local and a regional earthquake. Table S1 in the supplementary material summarises the earthquake parameters used in these tests. Displacement waveforms for two horizontal channels (N-S, *E*-W), and for each channel of our array were computed based on CRUST2.0 (Bassin et al., 2000), and ak135 (Kennett et al., 1995) velocity models, for the local and regional earthquakes respectively. The first time derivative was calculated in order to simulate velocity time series, which is proportional to strain rate, and all waveforms were rotated 20° from North to the East, in order to match the orientation of the array. Fig. S2 in the supplementary material shows examples of *P*-wave onsets with different levels of white noise added, and the obtained backazimuth and apparent slowness for each test based on the local synthetic earthquake.

Fig. 3 summarises mislocation errors for both synthetic earthquakes, showing that the backazimuth is always well resolved, but the apparent slowness shows greater uncertainty in all cases, especially in the case of the regional synthetic earthquake which may also be affected by the limited resolution of the array for such epicentral distances. Error ellipses are defined for each synthetic earthquake based on the mislocation errors with a semi-major axis of 30 km and 150 km for the local and regional synthetic earthquakes respectively, whereas, the semi-minor axis is 5 km and 20 km respectively, and the ellipsoid azimuth follows the event-station azimuth.

We then applied the method presented in Section 3 to two earthquakes, namely, the local 23 November 2021, M_L=3.4, Thiva earthquake (http://bbnet.gein.noa.gr/Events/2021/09/noa2021sqvcn_info.html), and a strong regional earthquake that occured on 12 October 2021, M_W=6.3, off the East coast of Crete (http://bbnet.gein.noa.gr/Events/2021/10/noa2021tzsju_info.html). Both earthquakes are shallow depth seismic events (< 15 km) but they show different azimuths with respect to the orientation of our DAS array.

We filtered the strain rate data, (i) from 0.5 Hz to 2.5 Hz, and (ii) from 1.0 Hz to 5.0 Hz using a zero phase shift Butterworth bandpass filter. Attempting to resolve backazimuth and slowness pairs using *P*-wave onsets for the two earthquakes did not show a clear source of maximum beam energy in either case, whereas, multiple sources of scattering were present, especially in the 1.0 Hz to 5.0 Hz *f-k* analysis. Since DAS is more sensitive in recording axial strain rate in the direction of the cable, *P*-waves showed low signal-to-noise ratio onsets, which yielded poor results in *f-k* analysis.

We repeated the above analysis, now focusing on the *S*-wave onsets (see Fig. S3 in the supplementary material), where we were able to resolve the backazimuth successfully in all cases (Fig. 4). Specifically, the backazimuth for the Thiva earthquake ranges from 290° to 300° at an apparent slowness of 0.32 s/km - 0.35 s/km, and for the Crete earthquake the highest beam energy is observed at a backazimuth range of 147° - 160° and an apparent slowness range of 0.33 s/km - 0.37 s/km. The higher the frequency band of the signal, the more sensitive to complex Earth structure is the wavefield, showing strong scattering effects. This is more evident in the case of the Crete earthquake (Fig. 4d) where the seismic waves travel through the Hellenic subduction zone.

By measuring the difference in arrival times of *P* and *S* onsets in the centre of the array as 6.1 s for the Thiva earthquake, and 50.1 s for the Crete earthquake, we were able to determine the earthquakes epicentral coordinates for a predetermined range of depth values since our method is based on prior rough estimates of the depth (see Table S2 in the supplementary material). Both of the studied earthquakes are shallow

depth (∼ 10 km) seismic events, thus, Fig. 4 summarises the results for shallow depth values, namely, at 0 km and 15 km depth. The obtained locations were compared to locations reported in the NOA Bulletin, calculated using a conventional approach based on picked phase arrival times (Lomax et al., 2000). In the case of the local Thiva earthquake the epicentres obtained in this study are only approximately 10 km away from the NOA epicentre, whereas, in the case of the Crete earthquake our epicentres land almost with the NOA error ellipse which represents one standard deviation (68% confidence level) around the mean of a normal statistic approximation of the PDF. Such differences in epicentral solutions are either due to the complexity of the Earth's structure, or most likely due to the longer distance with respect to the spacing of our array as shown by the synthetic tests, as the latter does not have the resolution to resolve the apparent slowness reliably, in conjunction with the level of signal coherency across the array.

## 5. Discussion and conclusions

In this study we used strain rate data from a Silixa iDAS interrogator which was connected to a fibre-optic cable in Athens, Greece, for one month. We tested the signal coherency across the cable and we carried out *f-k* analysis over two straight segments of the cable, forming an L-shaped array, in order to relocate two earthquakes in Greece, specifically, a small magnitude (M_L=3.4) local seismic event and a regional, strong earthquake (M_W=6.3) located off the east coast of Crete.

The local earthquake was relocated just 10 km away from the reported epicentre in the NOA Bulletin. Since error ellipse estimates are not included in the NOA Bulletin, we calculated error ellipses based on the model covariance matrix and phase arrivals in the NOA Bulletin (Bondár and Storchak, 2011, black dashed lines in Fig. 4). Since error ellipses are approximations of a complex misfit space depending on a priori data errors which are not always realistic, they mostly represent errors in the methodology, rather than true mislocations due to data uncertainties (Bondar, 2004). It is encouraging though that error ellipses based on true mislocation results from our synthetic test show some overlap with the error ellipse based on the NOA location for the Thiva local earthquake.

In the case of the regional earthquake, we were able to resolve the backazimuth of the earthquake, but the distance based on the apparent slowness obtained from the strain rate data yielded a location too far from the reported epicentre in the NOA Bulletin. Variations in the orientation of the fibre-optic cable are expected to add unknown phase changes into a certain degree. Moreover, the wrapping angle of the cable will influence the strain detection capability of the cable itself (Wuestefeld and Wilks, 2019), as well as large topographic changes and the Earth's structure heterogeneities will add substantial complexity in the observed strain measurements (Singh et al., 2019). This would affect the overall coherency of the recorded strain across the cable. In this context, it becomes obvious that every different segment of a fibre-optic cable behaves differently, furthermore, different cables deployed in different sites would have unique strain detection capabilities.

Several studies (i.e. Lindsey et al., 2017; Li et al., 2018; van den Ende and Ampuero, 2021), pointed out that the partial lack of coherency in DAS strain rate signals can potentially limit the ability of traditional frequency - wavenumber based techniques to successfully resolve the backazimuth and apparent slowness, unless strain rate is converted into particle velocity which requires additional processing, notably, integration and the estimation of seismic phase velocity. In our case where the spacing is too short the latter would increase waveform semblance, nevertheless, additional runtime would be necessary which would further decrease the possibility of using such a technique for fast and reliable preliminary locations.

Since the limitation of our array seems to be the slowness resolution, the use of an array with larger spacing could potentially improve the ability to accurately determine the apparent velocity of an incoming wavefield, nevertheless, the DAS signal coherency is expected to
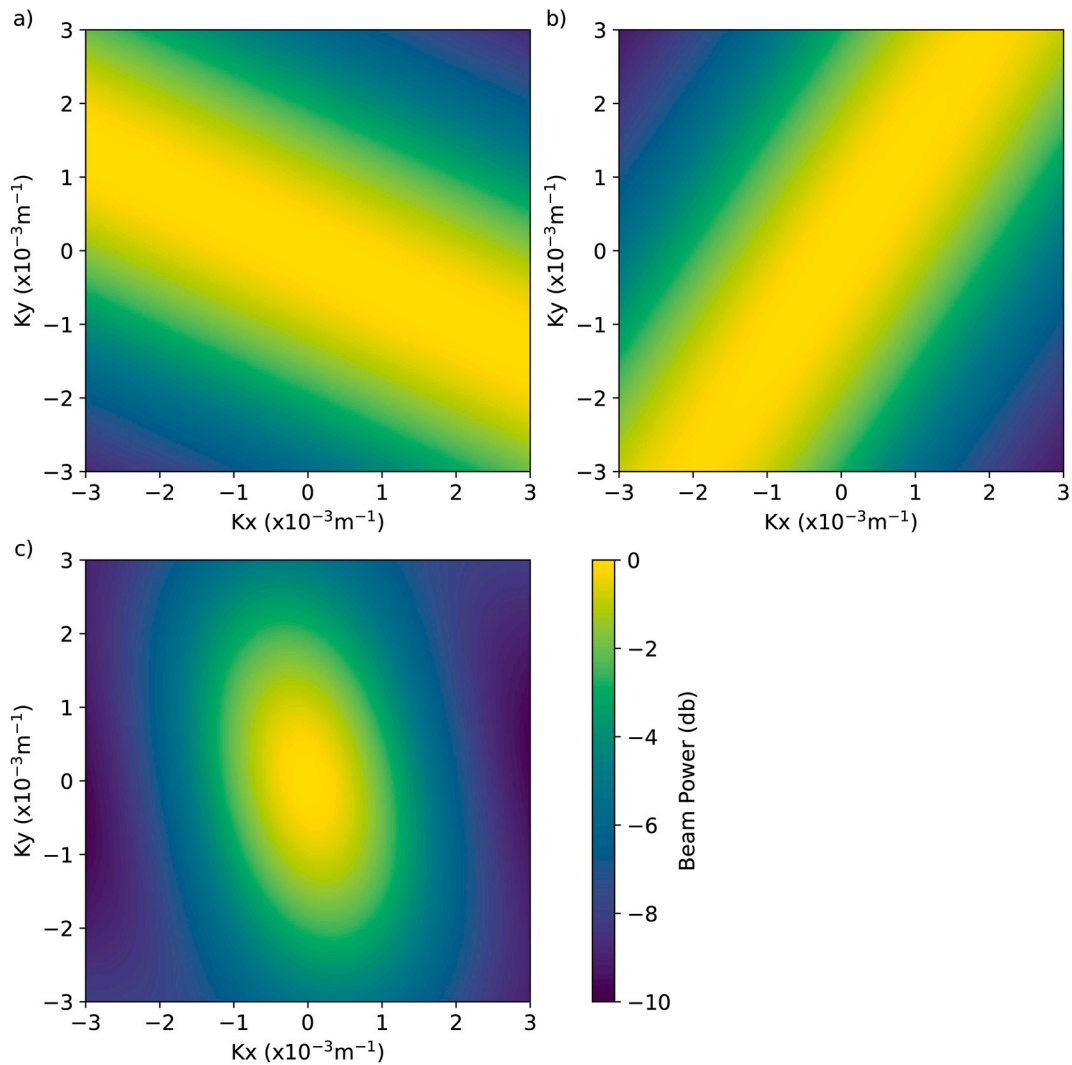
Fig. 2. Array transfer functions for the two linear segments of the DAS array used in this study, notably, the SW-NE oriented segment ranging from 810 m to 2300 m (a), the NW-SE oriented segment ranging from 2300 m to 3500 m (b), and the L-shaped array by combining the two previously mentioned segments (c). $K_x = f/V_{app,x}$ and $K_y = f/V_{app,y}$ denote the wavenumber in $(x,y) = (E,N)$ directions.
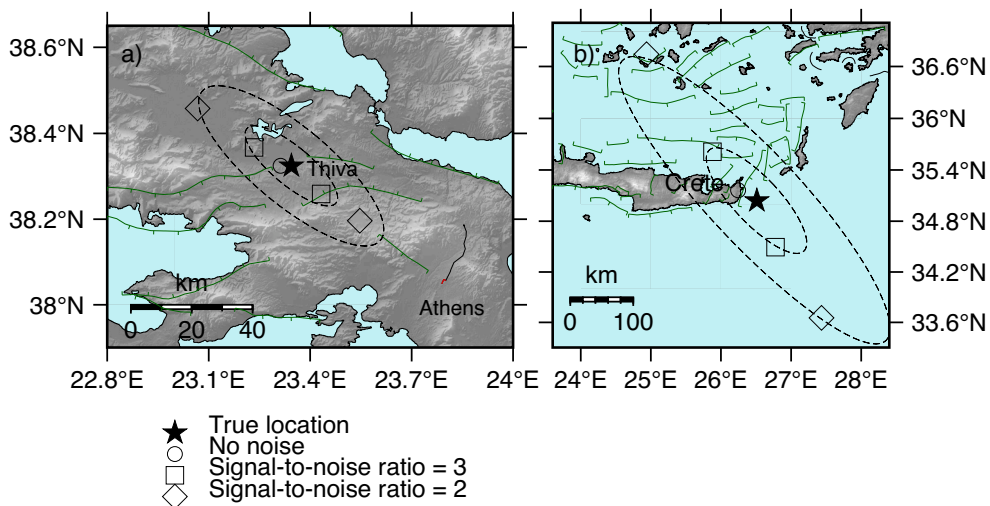
Fig. 3. Maps showing locations obtained from *f-k* analysis tests using the DAS array presented in Fig. 1, based on synthetic strain rate waveforms for an earthquake located in Thiva (a), and an earthquake located off the East coast of Crete (b), with respect to different levels of white noise added to the waveforms (see legend). Dashed lined error ellipses are defined based on the mislocated epicentres. The inner ellipse denotes errors for a signal-to-noise ratio equal to three, and the outer ellipse corresponds to signal-to-noise ratio equal to two.
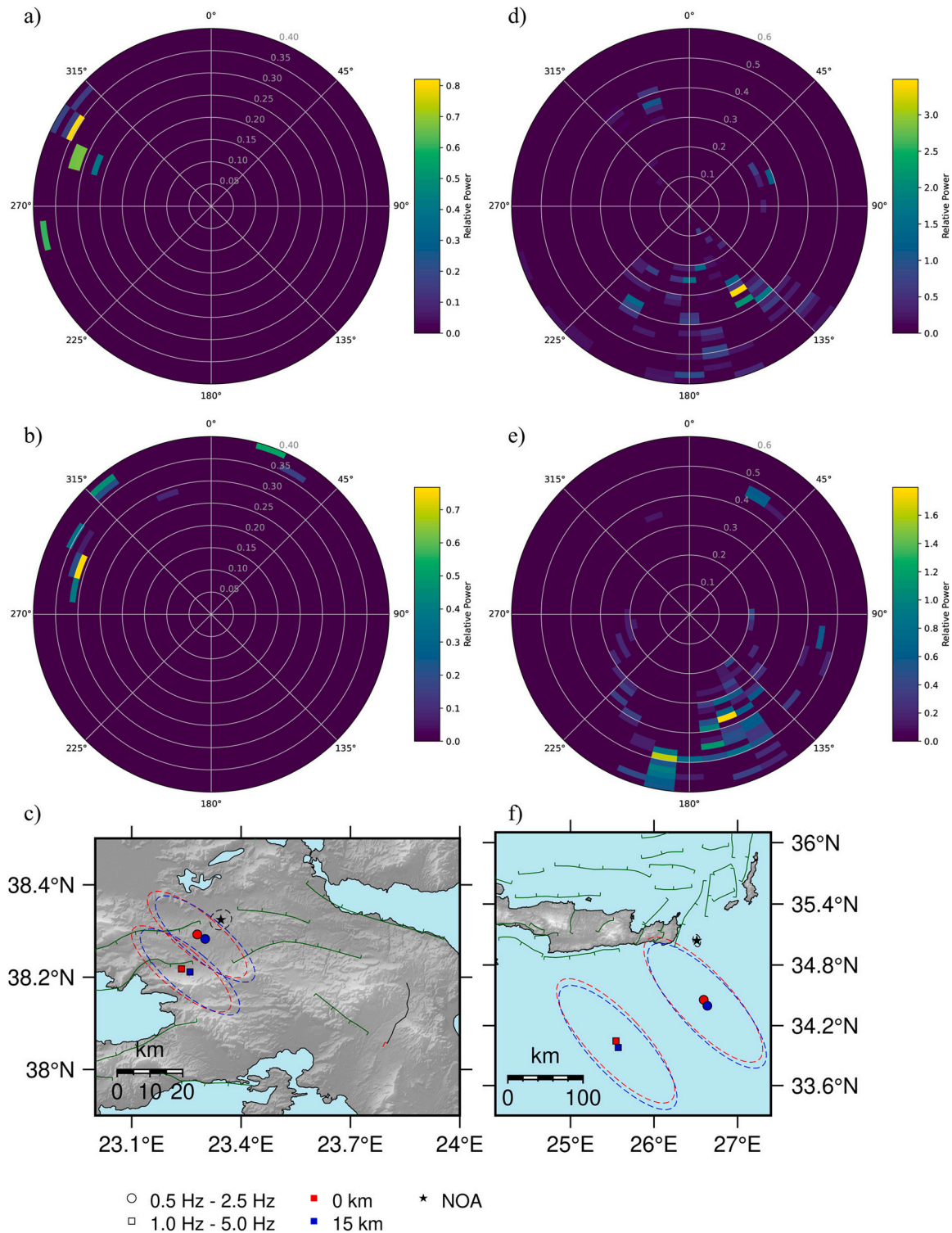
Fig. 4. Beamforming results based on *S*-wave *f-k* analysis for the two earthquakes tested in this study: (a) polar plot showing the relative power in bins of back-azimuth and slowness of the strain rate signal filtered between 0.5 Hz and 2.5 Hz for the M_L=3.4, Thiva earthquake; (b) same as in "a" but for the signal filtered between 1.0 Hz and 5.0 Hz; (c) map summarising the obtained locations in "a" and "b" for the M_L=3.4, Thiva earthquake; (d) polar plot showing the relative power in bins of backazimuth and slowness of the strain rate signal filtered between 0.5 Hz and 2.5 Hz for the M_W=6.3, off the East coast of Crete earthquake; (e) same as in "d" but for the signal filtered between 1.0 Hz and 5.0 Hz; (f) map summarising the obtained locations in "d" and "e" for the M_W=6.3, off the East coast of Crete earthquake. The locations reported in the NOA Bulletin are shown as black stars in the maps. The dashed line ellipses denote mislocation errors beased on synthetic tests (see text in Section 4). Circles represent locations based on the 0.5 Hz - 2.5 Hz frequency band *f-k* analysis, and squares represent locations based on the 1.0 Hz - 5.0 Hz *f-k* analysis. Locations based on 0 km and 15 km depth values are shown in red and blue, respectively. The trace of the fibre-optic cable is shown in black on the map in "c" for reference, and the segment used as a DAS array is highlighted in red. (For interpretation of the references to colour in this figure legend, the reader is referred to the web version of this article.)

deteriorate among channels with increased spacing. This trade-off between spatial extent of an array and signal coherency is key and may have different properties when considering different fibre-optic cables and array orientations.

CRediT authorship contribution statement

K. Lentas: Conceptualization, Methodology, Software, Writing – original draft. **D. Bowden:** Data curation, Software, Writing – review & editing. **N.S. Melis:** Writing – review & editing. **A. Fichtner:** Data curation, Writing – review & editing, Project administration. **M. Koroni:** Data curation. **A. Bogris:** Data curation, Project administration. **T. Nikas:** Data curation. **C. Simos:** Data curation. **I. Simos:** Data curation.

Declaration of Competing Interest

The authors declare that they have no known competing financial interests or personal relationships that could have appeared to influence the work reported in this paper.

Data availability

Data will be made available on request.

Acknowledgments

Appendix A. Supplementary data

Supplementary data to this article can be found online at https://doi.org/10.1016/j.pepi.2023.107109.

References

Agostinetti, N.P., Villa, A., Saccorotti, G., 2022. Distributed acoustic sensing as a tool for subsurface mapping and seismic event monitoring: a proof of concept. Solid Earth 13 (2), 449–468. URL. https://doi.org/10.5194/se-13-449-2022.

Ajo-Franklin, J.B., Dou, S., Lindsey, N.J., Monga, I., Tracy, C., Robertson, M., Tribaldos, V.R., Ulrich, C., Freifeld, B., Daley, T., Li, X., 2019. Distributed acoustic sensing using dark fiber for near-surface characterization and broadband seismic event detection. Sci. Rep. 9 (1) https://doi.org/10.1038/s41598-018-36675-8. URL.

Aki, K., Richards, P.G., 1981. Quantitative seismology, theory and methods. Volume i: 557 pp., 169 illustrations. Volume II: 373 pp., 116 illustrations. San Francisco: freeman. Price: volume i, u.s. 35.00 volume II, u.s. 35.00. ISBN 0 7167 1058 7 (vol. i), 0 7167 1059 5 (vol. II). Geol. Mag. 118 (2). URL. https://doi.org/10.1017/s0016756800034439. Vol. I 557 pp; Vol. II 560-932 pp.

Bassin, C., Laske, G., Masters, G., 2000. The current limits of resolution for surface wave tomography in north america. eos trans agu 81 f897. Eos 81, F897.

Beyreuther, M., Barsch, R., Krischer, L., Megies, T., Behr, Y., Wassermann, J., 2010. Obspy: a python toolbox for seismology. Seismol. Res. Lett. 81, 530–533.

Bogris, A., Nikas, T., Simos, C., Simos, I., Lentas, K., Melis, N.S., Fichtner, A., Bowden, D., Smolinski, K., Mesaritakis, C., Chochliouros, I., 2022. Sensitive seismic sensors based on microwave frequency fiber interferometry in commercially deployed cables. Sci. Rep. 12 (1) https://doi.org/10.1038/s41598-022-18130-x. URL.

Bondar, I., 2004. Collection of a reference event set for regional and teleseismic location calibration. Bull. Seismol. Soc. Am. 94 (4), 1528–1545. URL. https://doi.org/10.1785/012003128.

Bondár, I., Storchak, D., 2011. Improved location procedures at the international seismological Centre. Geophys. J. Int. 186 (3), 1220–1244. URL. https://doi.org/10.1111/j.1365-246x.2011.05107.x.

Booth, A.D., Christoffersen, P., Schoonman, C., Clarke, A., Hubbard, B., Law, R., Doyle, S. H., Chudley, T.R., Chalari, A., 2020. Distributed acoustic sensing of seismic properties in a borehole drilled on a fast-flowing greenlandic outlet glacier. Geophys. Res. Lett. 47 (13) https://doi.org/10.1029/2020gl088148. URL.

Bowden, D.C., Fichtner, A., Nikas, T., Bogris, A., Simos, C., Smolinski, K., Koroni, M., Lentas, K., Simos, I., Melis, N.S., 2022. Linking distributed and integrated fiber-optic sensing. Geophys. Res. Lett. 49 (16) https://doi.org/10.1029/2022gl098727. URL.

Capon, J., Greenfield, R., Kolker, R., 1967. Multidimensional maximum–likelihood processing of a large aperture seismic array. Proc. IEEE 55 (2), 192–211. URL. https://doi.org/10.1109/proc.1967.5439.

Daley, T.M., Freifeld, B.M., Ajo-Franklin, J., Dou, S., Pevzner, R., Shulakova, V., Kashikar, S., Miller, D.E., Goetz, J., Henninges, J., Lueth, S., 2013. Field testing of fiber-optic distributed acoustic sensing (DAS) for subsurface seismic monitoring. Lead. Edge 32 (6), 699–706. URL. https://doi.org/10.1190/tle32060699.1.

Fang, G., Li, Y.E., Zhao, Y., Martin, E.R., 2020. Urban near-surface seismic monitoring using distributed acoustic sensing. Geophys. Res. Lett. 47 (6) https://doi.org/10.1029/2019gl086115. URL.

Fichtner, A., Klaasen, S., Thrastarson, S., Çubuk-Sabuncu, Y., Paitz, P., Jónsdóttir, K., 2022. Fiber-optic observation of volcanic tremor through floating ice sheet resonance. Seism. Recor. 2 (3), 148–155. URL. https://doi.org/10.1785/0320220010.

Hartog, A.H., 2017. An Introduction to Distributed Optical Fibre Sensors. CRC Press. https://doi.org/10.1201/9781315119014. URL.

Hudson, T.S., Baird, A.F., Kendall, J.M., Kufner, S.K., Brisbourne, A.M., Smith, A.M., Butcher, A., Chalari, A., Clarke, A., 2021. Distributed acoustic sensing (DAS) for natural microseismicity studies: a case study from Antarctica. J. Geophys. Res. Solid Earth 126 (7). https://doi.org/10.1029/2020jb021493. URL.

Hunter, J.D., 2007. Matplotlib: a 2d graphics environment. Compu. Sci. Eng. 9 (3), 90–95.

Ide, S., Araki, E., Matsumoto, H., 2021. Very broadband strain-rate measurements along a submarine fiber-optic cable off Cape Muroto, nankai subduction zone, Japan. Earth, Planets and Sspace 73 (1). https://doi.org/10.1186/s40623-021-01385-5. URL.

Ishii, M., Shearer, P.M., Houston, H., Vidale, J.E., 2005. Extent, duration and speed of the 2004 Sumatra–andaman earthquake imaged by the hi-net array. Nature 435 (7044), 933–936. URL. https://doi.org/10.1038/nature03675.

Jousset, P., Reinsch, T., Ryberg, T., Blanck, H., Clarke, A., Aghayev, R., Hersir, G.P., Henninges, J., Weber, M., Krawczyk, C.M., 2018. Dynamic strain determination using fibre-optic cables allows imaging of seismological and structural features. Nat. Commun. 9 (1) https://doi.org/10.1038/s41467-018-04860-y. URL.

Karney, C.F.F., 2012. Algorithms for geodesics. J. Geod. 87 (1), 43–55. URL. https://doi.org/10.1007/s00190-012-0578-z.

Kennett, B.L.N., Engdahl, E.R., Buland, R., 1995. Constraints on seismic velocities in the earth from traveltimes. Geophys. J. Int. 122 (1), 108–124. URL. https://doi.org/10.1111/j.1365-246x.1995.tb03540.x.

Klaasen, S., Paitz, P., Lindner, N., Dettmer, J., Fichtner, A., 2021. Distributed acoustic sensing in volcano-glacial environments—mount meager, British columbia. J. Geophys. Res. Solid Earth 126 (11). https://doi.org/10.1029/2021jb022358. URL.

Kværna, T., Ringdal, F., 1986. Stability of Various f-k Estimation Techniques. URL. https://www.norsar.no/doi/p.1986.0001.

Li, Z., Peng, Z., Hollis, D., Zhu, L., McClellan, J., 2018. High-resolution seismic event detection using local similarity for large-n arrays. Sci. Rep. 8 (1) https://doi.org/10.1038/s41598-018-19728-w. URL.

Lindsey, N.J., Martin, E.R., 2021. Fiber-optic seismology. Annu. Rev. Earth Planet. Sci. 49 (1), 309–336. URL. https://doi.org/10.1146/annurev-earth-072420-065213.

Lindsey, N.J., Martin, E.R., Dreger, D.S., Freifeld, B., Cole, S., James, S.R., Biondi, B.L., Ajo-Franklin, J.B., 2017. Fiber-optic network observations of earthquake wavefields. Geophys. Res. Lett. 44 (23) https://doi.org/10.1002/2017gl075722. URL.

Lindsey, N.J., Rademacher, H., Ajo-Franklin, J.B., 2020. On the broadband instrument response of fiber-optic DAS arrays. J. Geophys. Res. Solid Earth 125 (2). https://doi.org/10.1029/2019jb018145. URL.

Lior, I., Sladen, A., Mercerat, D., Ampuero, J.-P., Rivet, D., Sambolian, S., 2021. Strain to ground motion conversion of distributed acoustic sensing data for earthquake magnitude and stress drop determination. Solid Earth 12 (6), 1421–1442. URL. https://doi.org/10.5194/se-12-1421-2021.

Lomax, A., Virieux, J., Volant, P., Berge-Thierry, C., 2000. Probabilistic earthquake location in 3d and layered models. In: Advances in Seismic Event Location. Springer Netherlands, pp. 101–134. URL. https://doi.org/10.1007/978-94-015-9536-0_5.

Mateeva, A., Mestayer, J., Cox, B., Kiyashchenko, D., Wills, P., Lopez, J., Grandi, S., Hornman, K., Lumens, P., Franzen, A., Hill, D., Roy, J., 2012. Advances in distributed acoustic sensing (DAS) for VSP. In: SEG Technical Program Expanded Abstracts 2012. Soc. Explorat. Geophys. https://doi.org/10.1190/segam2012-0739.1. URL.

Matsumoto, H., Araki, E., Kimura, T., Fujie, G., Shiraishi, K., Tonegawa, T., Obana, K., Arai, R., Kaiho, Y., Nakamura, Y., Yokobiki, T., Kodaira, S., Takahashi, N., Ellwood, R., Yartsev, V., Karrenbach, M., 2021. Detection of hydroacoustic signals on a fiber-optic submarine cable. Sci. Rep. 11 (1) https://doi.org/10.1038/s41598-021-82093-8. URL.

Meng, L., Allen, R.M., Ampuero, J.-P., 2014. Application of seismic array processing to earthquake early warning. Bull. Seismol. Soc. Am. 104 (5), 2553–2561. URL. https://doi.org/10.1785/0120130277.

Mykkeltveit, S., Fyen, J., Ringdal, F., Kværna, T., 1990. Spatial characteristics of the NORESS noise field and implications for array detection processing. Phys. Earth Planet. Inter. 63 (3-4), 277–283. URL. https://doi.org/10.1016/0031-9201(90)90028-v.

Näsholm, S.P., Iranpour, K., Wuestefeld, A., Dando, B.D.E., Baird, A.F., Oye, V., 2022. Array signal processing on distributed acoustic sensing data: directivity effects in slowness space. J. Geophys. Res. Solid Earth 127 (2). https://doi.org/10.1029/2021jb023587. URL.

Nishimura, T., Emoto, K., Nakahara, H., Miura, S., Yamamoto, M., Sugimura, S., Ishikawa, A., Kimura, T., 2021. Source location of volcanic earthquakes and subsurface characterization using fiber-optic cable and distributed acoustic sensing system. Sci. Rep. 11 (1) https://doi.org/10.1038/s41598-021-85621-8. URL.

Paitz, P., Edme, P., Gräff, D., Walter, F., Doetsch, J., Chalari, A., Schmelzbach, C., Fichtner, A., 2020. Empirical investigations of the instrument response for distributed acoustic sensing (DAS) across 17 octaves. Bull. Seismol. Soc. Am. 111 (1), 1–10. URL. https://doi.org/10.1785/0120200185.

Pirli, M., Voulgaris, N., Chira, A., Makropoulos, K., 2006. The march 2004 Kalamata seismic sequence: a case of efficient seismicity monitoring in the area of peloponnese, southern Greece, by the Tripoli seismic array. J. Seismol. 11 (1), 59–72. URL. https://doi.org/10.1007/s10950-006-9037-8.

Schweitzer, J., Krüger, F., 2011. Foreword. J. Seismol. 15 (3), 429–430. URL. https://doi.org/10.1007/s10950-011-9241-z.

Schweitzer, J., Fyen, J., Mykkeltveit, S., Gibbons, S.J., Pirli, M., Kühn, D., Kvärna, T., 2012. Seismic arrays. New Manual of Seismological Observatory practice 2 (NMSOP2). URL. https://gfzpublic.gfz-potsdam.de/pubman/item/item_43213.

Singh, S., Capdeville, Y., Igel, H., 2019. Correcting wavefield gradients for the effects of local small-scale heterogeneities. Geophys. J. Int. https://doi.org/10.1093/gji/ggz479.

Song, Z., Zeng, X., Xie, J., Bao, F., Zhang, G., 2021. Sensing shallow structure and traffic noise with fiber-optic internet cables in an urban area. Surv. Geophys. 42 (6), 1401–1423. URL. https://doi.org/10.1007/s10712-021-09678-w.

Spica, Z.J., Perton, M., Martin, E.R., Beroza, G.C., Biondi, B., 2020. Urban seismic site characterization by fiber-optic seismology. J. Geophys. Res. Solid Earth 125 (3). https://doi.org/10.1029/2019jb018656. URL.

van den Ende, M.P.A., Ampuero, J.-P., 2021. Evaluating seismic beamforming capabilities of distributed acoustic sensing arrays. Solid Earth 12 (4), 915–934. URL. https://doi.org/10.5194/se-12-915-2021.

Wessel, P., Smith, W.H.F., Scharroo, R., Luis, J., Wobbe, F., 2013. Generic mapping tools: improved version released. EOS Trans. Am. Geophys. Union 94 (45), 409–410.

Wuestefeld, A., Wilks, M., 2019. How to twist and turn a fiber: performance modeling for optimal DAS acquisitions. Lead. Edge 38 (3), 226–231. URL. https://doi.org/10.1190/tle38030226.1.

Zhu, T., Shen, J., Martin, E.R., 2021. Sensing earth and environment dynamics by telecommunication fiber-optic sensors: an urban experiment in Pennsylvania, USA. Solid earth 12 (1), 219–235. URL. https://doi.org/10.5194/se-12-219-2021.